Supporting Information

^{57}Fe Nuclear Resonance Vibrational Spectroscopic Studies of Tetranuclear Iron Clusters Bearing Terminal Iron(III)-Oxido/Hydroxido Moieties

Jin Xiong,[a] Christopher Reed,[b] Barbara Lavina,[c,d] Michael Y. Hu,[c] Jiyong Zhao,[c] Ercan E. Alp,[c] Theodor Agapie,[b]* and Yisong Guo[a]*

[a] *Department of Chemistry, Carnegie Mellon University, Pittsburgh, PA 15213, USA*

[b] *Division of Chemistry and Chemical Engineering, California Institute of Technology, CA 91125, USA*

[c] *Advanced Photon Source, Argonne National Laboratory, Argonne, Illinois 60439, USA*

[d] *Center for Advanced Radiation Source, University of Chicago, Chicago, Illinois, 60439, USA*

Synthesis Procedures: The [Fe_4] clusters were prepared using previously reported procedures.[1] Isotopically enriched clusters were derived from $^{57}Fe(OAc)_2$ and $^{57}Fe(OTf)_2$ • 2 MeCN made from ^{57}Fe powder and K^{18}OH and PhI^{18}O made from $^{18}OH_2$.

Preparation of NRVS Samples: Solid NRVS sample holders were covered on one side with Kapton tape and were laid out on to a kimwipe for a clean surface. The well-ground powder of each sample was suspended into *Nujol*, transferred into a special designed polyoxymethylene sample holder which has a *Kepton* tape window allowing X-ray to penetrate in. Then the whole cup was frozen with a cold aluminum block, and further stored in liquid nitrogen.

^{57}Fe Nuclear Resonant Vibrational Spectroscopy: The experiment was conducted at beamline 3ID at the Advanced Photon Source (APS), Argonne National Laboratory, IL, USA. The instrument equipped with a liquid helium flow cryostat and the sample was cooled with a copper cold finger, thus samples were maintained at a cryogenic temperature of approximately 20 K. The temperature for individual spectra were calculated using the ratio of anti-Stokes to Stokes intensity according to $S(-E) = S(E)\exp(-E/kT)$ and were generally in the range of 40 K to 80 K. The monochromators provide a high energy resolution of ~ 1 meV by employing a cryo-cooled silicon (1,1,1) double crystal with 1.1 eV bandpass, followed by two separate Si(4,0,0) and Si(10,6,4) channel-cut crystals in a symmetric geometry.[2] Single avalanche photodiode (APD) detector was used at both forward and perpendicular direction. A solid $K_2MgFe(CN)_6$ sample was used as energy calibration standard with a reference point of its Fe-C(ν7) vibrational mode reported at 74 meV.[3,4] The resolution function was collected by recording the delayed nuclear fluorescence at the forward direction simultaneously when the scattering photons were recorded at the perpendicular direction. The spectra were recorded between -50 meV and +180 meV, 3 sec/step for each scan with a step size of 0.25 meV. Each scan required about 50 minutes, and all scans were added and normalized to the intensity of the incident beam. The program *PHEONIX-3.0.3* was employed to process the data and derive the ^{57}Fe PVDOS.[5]

DFT calculations:

General method: Unless specified, the present broken-symmetry (BS) DFT calculations were carried out using Gaussian 16 Rev C01 with its tight optimization threshold.[6] B3LYP functional together were employed.[7,8] All the atoms were described by TZVP basis sets.[9,10] For thermochemistry calculated by DFT, the conductor-like solvation model of THF, developed in the framework of the polarizable continuum model, was utilized in both optimization and frequency analysis.[11]

^{57}Fe PVDOS calculation: The crystal structure of each complex was optimized with DFT method. Optimization threshold was set to tight. Frequency analysis was followed by optimization to generate normal modes of vibration and their associated frequencies. The ^{57}Fe PVDOS was generated by using an in-house program that extracts the Cartesian normal mode displacements obtained by DFT frequency calculations and converts them into ^{57}Fe mode composition factor $e^2_{Fe,\alpha}$ based on the following equation:[12]

$$e^2_{Fe,\alpha} = \frac{m_{Fe} r^2_{Fe,\alpha}}{\sum_{\alpha} m_i r^2_{i,\alpha}} \qquad \text{(Eq. 1)}$$

where m_i and $r^2_{i,\alpha}$ are the mass of atom i and its mean square motion in mode α. The obtained ^{57}Fe mode composition factor was further used to reconstruct ^{57}Fe PVDOS spectra to compare with experimental data according to the following equation:[13]

$$D_{Fe}(\bar{\nu}) = \sum_{\alpha} e^2_{Fe,\alpha} \ell(\bar{\nu} - \bar{\nu}_{\alpha}) \qquad \text{(Eq. 2)}$$

where the line shape function $\ell(\bar{\nu} - \bar{\nu}_{\alpha})$ was generated by using a 10 cm^{-1} gaussian broadening to mimic the experimental energy resolution.

Structure Optimization Details: The spin coupling scheme is one of the major factors dominate the optimized geometry. Different coupling schemes yield to different PVDOS spectra. Consequently, the Fe-O/OH stretching energy also varies. As magnetic data suggests, the most possible coupling scheme is that the apical HS Fe^{III} antiparallelly aligned its spin with the bottom three HS Fe^{III} or HS Fe^{II}. Therefore, we employed this spin coupling scheme for all the complexes. In regard to DFT functionals, we started our optimization with BP86 functionals as it worked very well for PVDOS spectra calculation of mononuclear iron complexes,[14] while the B3LYP functionals always overestimate the Fe-L bond lengths. However, the results suggest that BP86 failed to mimic the asymmetric bottom $Fe_3(\mu_4O)$ moiety suggested by crystal structure. For example, for [Fe^{II}Fe$^{III}_2$OFe^{III}]-O, the BP86-optimized geometry shows almost identical Fe-μ_4O bond lengths (2.06, 2.06 and 2.07 Å, respectively), while the crystal structure reveals unequal Fe-μ_4O bond lengths (1.93, 1.95 and 2.15 Å, respectively). However, hybrid functionals, e.g. B3LYP, fixed this problem, thus successfully mimicking the unequal Fe-μ_4O bond lengths. For [Fe^{II}Fe$^{III}_2$OFe^{III}]-O, the bottom Fe-μ_4O bond lengths are 1.95, 1.96 and 2.20 Å, respectively. This suggests that Hartree-Fock exchange may be important to understand the electronic structure of such tetranuclear iron clusters by correcting the charge/spin delocalization among the Fe_3O moiety.

Therefore, we employed B3LYP functionals in our calculations. The coordinates of optimized geometries are listed in a separated SI file (Optimized_geometries.txt).

Table S1. Comparisons of the selected bond lengths of the [Fe_4] clusters from the DFT calculated and XRD determined structures.[a]

	$[Fe^{III}_3OFe^{III}]$-O [b]	$[Fe^{III}_3OFe^{III}]$-OH [b]	$[Fe^{II}Fe^{III}_2OFe^{III}]$-O [c]		$[Fe^{II}Fe^{III}_2OFe^{III}]$-OH [c]		$[Fe^{II}_2Fe^{III}OFe^{III}]$-O [c]		$[Fe^{II}_2Fe^{III}OFe^{III}]$-OH [c]		$[Fe^{II}_3OFe^{III}]$-OH	
	DFT	DFT	*XRD*	DFT	*XRD*	DFT	*XRD*	DFT	*XRD*	DFT	*XRD*	DFT
Fe1-O(H)	1.783	1.886	*1.796*	1.781	*1.879*	1.901	*1.817*	1.785	*1.907*	1.925	*1.937*	1.958
Fe1-N_{eq} (Avg)	2.1	2.088	*2.090*	2.108	*2.063*	2.097	*2.098*	2.132	*2.084*	2.114	*2.125*	2.155
Fe1-μ_4O	2.128	2.014	*2.049*	2.103	*1.948*	1.980	*1.965*	2.058	*1.889*	1.929	*1.837*	1.866
Fe2-μ_4O	2.021	2.091	*2.155*	2.196	*2.148*	2.213	*2.139*	2.167	*2.142*	2.182	*2.109*	2.136
Fe3-μ_4O	2.021	2.078	*1.947*	1.957	*1.971*	1.990	*2.05*	2.133	*2.101*	2.173	*2.102*	2.132
Fe4-μ_4O	2.021	2.007	*1.927*	1.951	*2.002*	2.008	*1.967*	1.878	*1.952*	1.923	*2.089*	2.095
Fe_{234}-μ_4O (Avg)	2.021	2.059	*2.010*	2.034	*2.040*	2.070	*2.052*	2.059	*2.065*	2.093	*2.100*	2.121
Fe2-L (Avg)	2.121	2.127	*2.136*	2.186	*2.118*	2.192	*2.150*	2.187	*2.130*	2.190	*2.142*	2.194
Fe3-L (Avg)	2.121	2.120	*2.068*	2.117	*2.057*	2.112	*2.112*	2.188	*2.124*	2.190	*2.139*	2.193
Fe4-L (Avg)	2.121	2.106	*2.051*	2.114	*2.076*	2.110	*2.093*	2.125	*2.077*	2.114	*2.138*	2.194
Fe_{234}-L (Avg)	2.121	2.117	*2.085*	2.139	*2.084*	2.138	*2.118*	2.167	*2.110*	2.165	*2.140*	2.194

[a] The bond lengths of XRD determined structures were taken from [1]. Fe1 represents the apical iron center of these complexes and Fe2, Fe3, and Fe4 represent the base iron centers of these complexes.

[b] No XRD data are available for this complex.

[c] the complex studied by ^{57}Fe NRVS in this work.

Table S2. The DFT calculated spin population of the iron centers of the [Fe_4] clusters.[a]

	Fe1	Fe2	Fe3	Fe4
[$Fe^{III}_3OFe^{III}$]-O	-4.03	+4.12	+4.12	+4.12
[$Fe^{III}_3OFe^{III}$]-OH	-4.17	+4.13	+4.23	+4.11
[$Fe^{II}Fe^{III}_2OFe^{III}$]-O [b]	-4.01	+3.81	+4.15	+4.15
[$Fe^{II}Fe^{III}_2OFe^{III}$]-OH [b]	-4.18	+3.80	+4.17	+4.17
[$Fe^{II}_2Fe^{III}OFe^{III}$]-O [b]	-4.02	+3.80	+3.80	+4.12
[$Fe^{II}_2Fe^{III}OFe^{III}$]-OH [b]	-4.18	+3.79	+3.80	+4.16
[$Fe^{II}_3OFe^{III}$]-OH	-4.19	+3.77	+3.77	+3.77

[a] Fe1 represents the apical iron center of these complexes and Fe2, Fe3, and Fe4 represent the base iron centers of these complexes.

[b] The complexes studied by ^{57}Fe NRVS in this work.

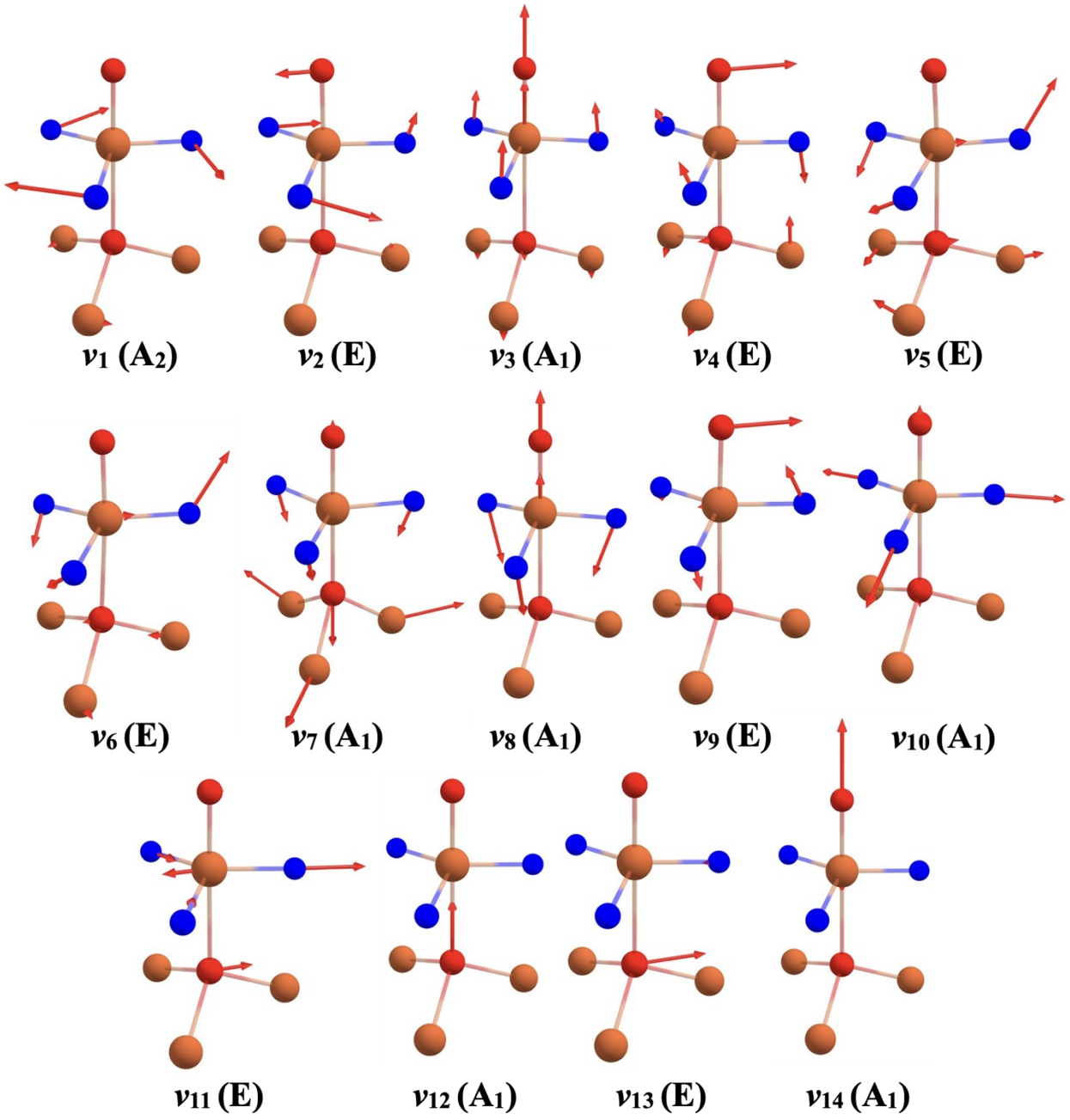

Figure S1. Normal modes of vibration of a $OFe(X_3)(YZ_3)$ type molecule in a C_{3v} symmetry derived from DFT calculations. For each mode, the corresponding irreducible representation under C_{3v} symmetry is indicated.

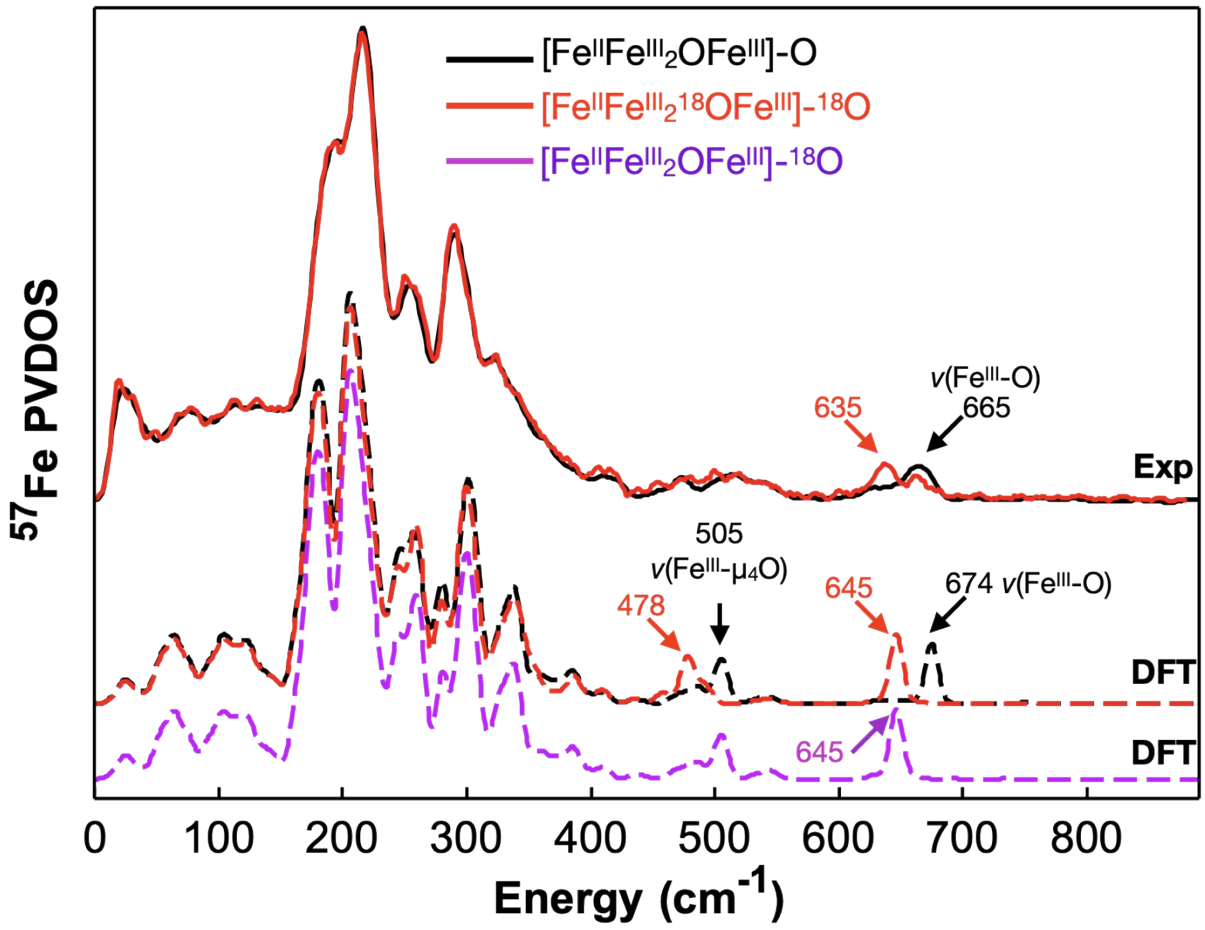

Figure S2. ^{57}Fe PVDOS experimental and DFT calculated spectra from [$Fe^{II}Fe^{III}_2OFe^{III}$]-O. Top: the experimental spectra of [$Fe^{II}Fe^{III}_2{}^{16}OFe^{III}$]-^{16}O (black) and [$Fe^{II}_2Fe^{III}{}^{18}OFe^{III}$]-^{18}O (red). Bottom: The DFT calculated spectra of [$Fe^{II}Fe^{III}_2{}^{16}OFe^{III}$]-^{16}O (black), [$Fe^{II}Fe^{III}_2{}^{18}OFe^{III}$]-^{18}O (red), and [$Fe^{II}Fe^{III}_2{}^{16}OFe^{III}$]-^{18}O (purple). The frequencies of ν(Fe^{III}-O) and ν(Fe^{III}-μ_4O) in these complexes are indicated in the figure. ν(Fe^{III}-^{18}O) is not affected by the isotope (^{16}O or ^{18}O) of μ_4O.

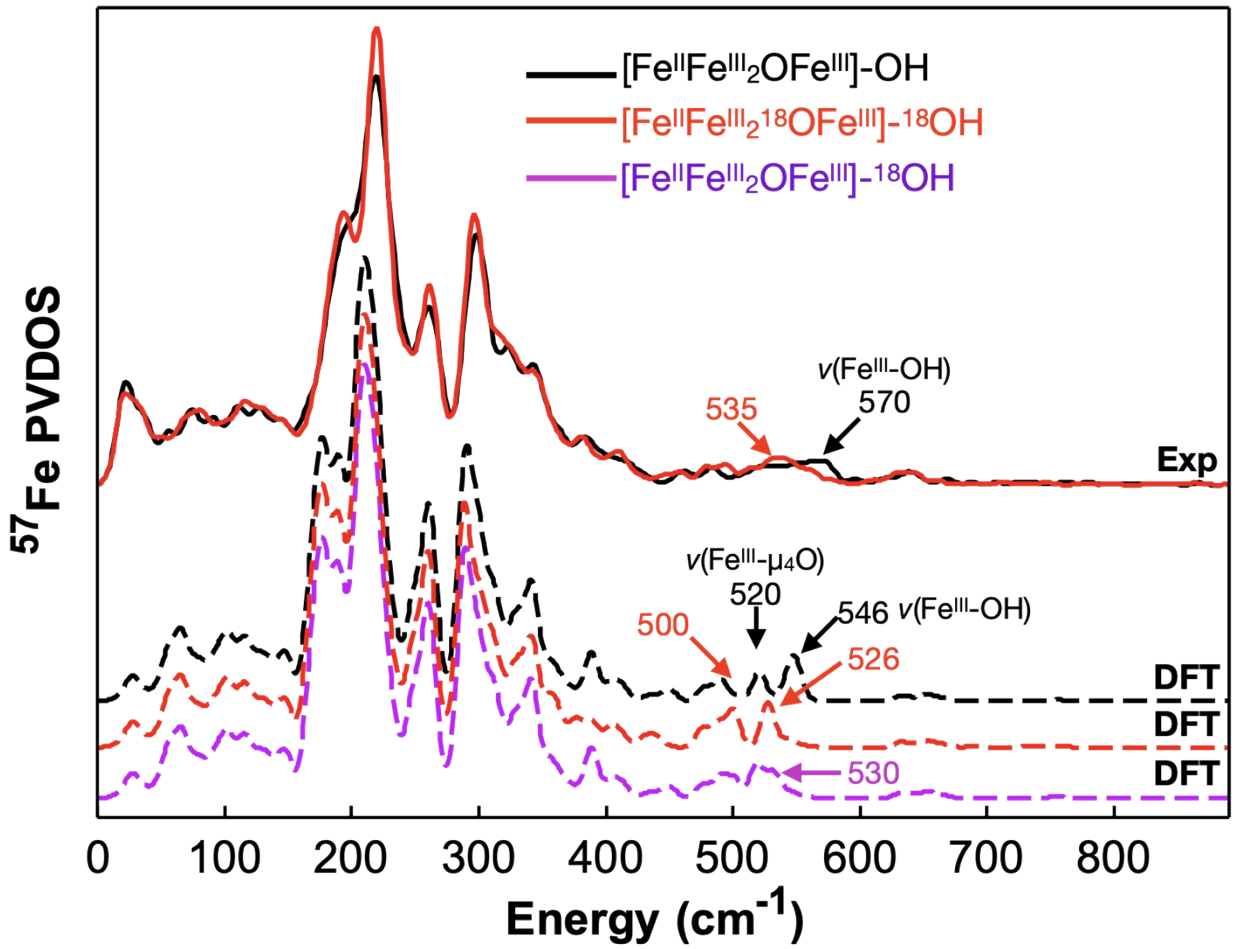

Figure S3. ^{57}Fe PVDOS experimental and DFT calculated spectra from [$Fe^{II}Fe^{III}_2OFe^{III}$]-OH. Top: the experimental spectra of [$Fe^{II}Fe^{III}_2{}^{16}OFe^{III}$]-^{16}OH (black) and [$Fe^{II}Fe^{III}_2{}^{18}OFe^{III}$]-^{18}OH (red). Bottom: The DFT calculated spectra of [$Fe^{II}Fe^{III}_2{}^{16}OFe^{III}$]-^{16}OH (black), [$Fe^{II}Fe^{III}_2{}^{18}OFe^{III}$]-^{18}OH (red), and [$Fe^{II}Fe^{III}_2{}^{16}OFe^{III}$]-^{18}OH (purple). The frequencies of ν(Fe^{III}-OH) and ν(Fe^{III}-μ_4O) in these complexes are indicated in the figure. ν(Fe^{III}-^{18}OH) is only slightly affected by the isotope (^{16}O or ^{18}O) of μ_4O.

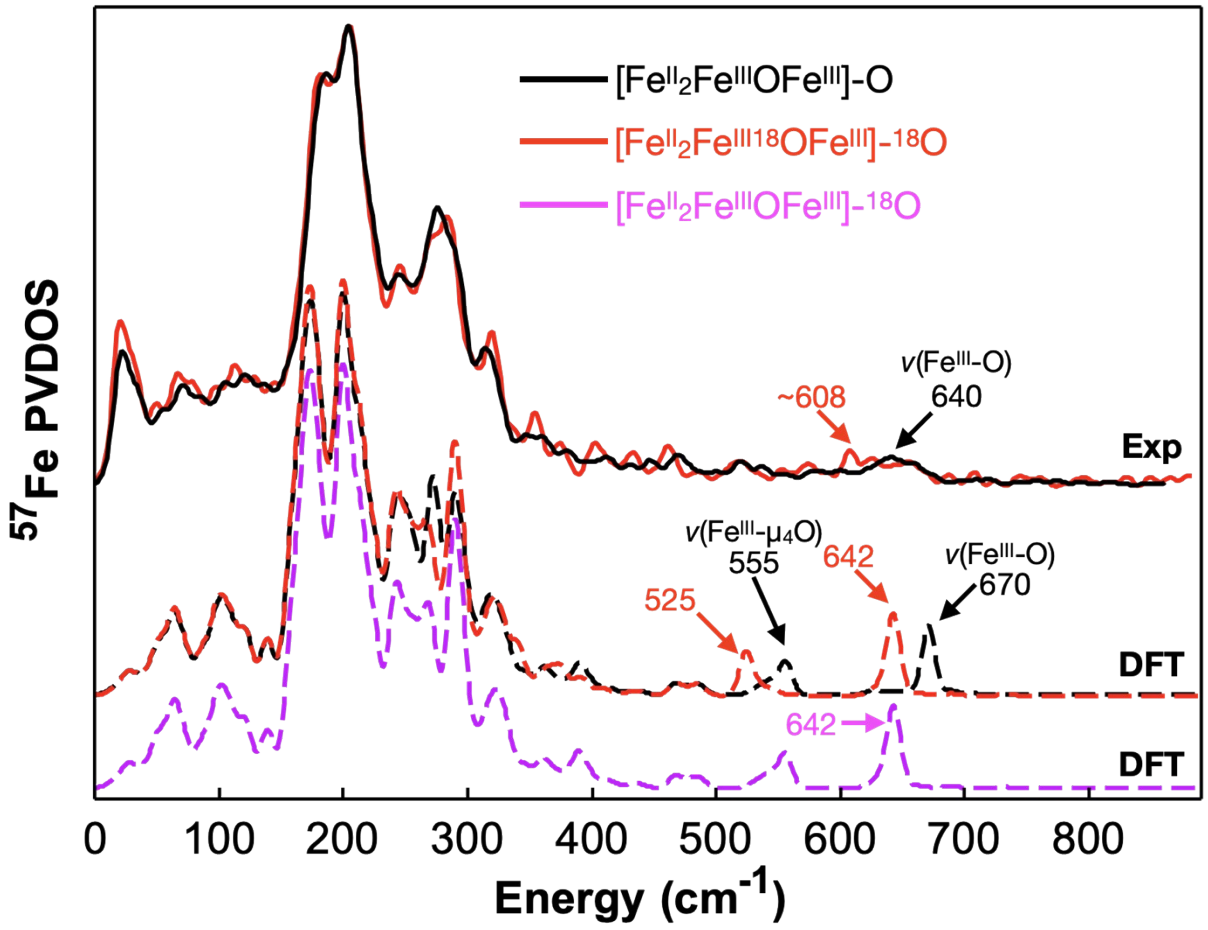

Figure S4. ^{57}Fe PVDOS experimental and DFT calculated spectra from [Fe$^{II}_2$Fe^{III}OFe^{III}]-O. Top: the experimental spectra of [Fe$^{II}_2$Fe^{III16}OFe^{III}]-^{16}O (black) and [Fe$^{II}_2$Fe^{III18}OFe^{III}]-^{18}O (red). Bottom: The DFT calculated spectra of [Fe$^{II}_2$Fe^{III16}OFe^{III}]-^{16}O (black), [Fe$^{II}_2$Fe^{III18}OFe^{III}]-^{18}O (red), and [Fe$^{II}_2$Fe^{III16}OFe^{III}]-^{18}O (purple). The frequencies of ν(Fe^{III}-O) and ν(Fe^{III}-μ_4O) in these complexes are indicated in the figure. ν(Fe^{III}-^{18}O) is not affected by the isotope (^{16}O or ^{18}O) of μ_4O.

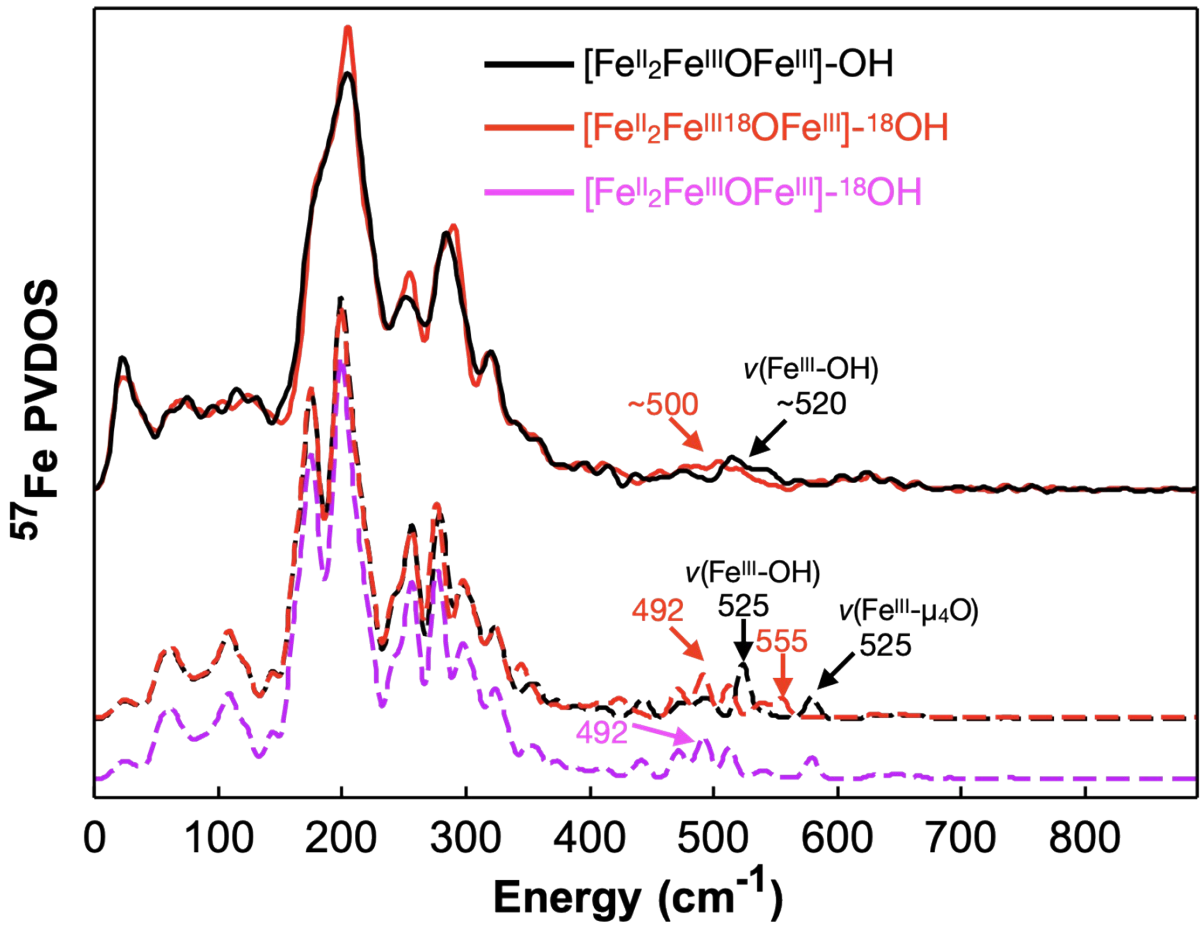

Figure S5. ^{57}Fe PVDOS experimental and DFT calculated spectra from [Fe$^{II}_2$Fe^{III}OFe^{III}]-OH. Top: the experimental spectra of [Fe$^{II}_2$Fe^{III16}OFe^{III}]-^{16}OH (black) and [Fe$^{II}_2$Fe^{III18}OFe^{III}]-^{18}OH (red). Bottom: The DFT calculated spectra of [Fe$^{II}_2$Fe^{III16}OFe^{III}]-^{16}OH (black), [Fe$^{II}_2$Fe^{III18}OFe^{III}]-^{18}OH (red), and [Fe$^{II}_2$Fe^{III16}OFe^{III}]-^{18}OH (purple). The frequencies of ν(Fe^{III}-OH) and ν(Fe^{III}-μ_4O) in these complexes are indicated in the figure. ν(Fe^{III}-^{18}OH) is only slightly affected by the isotope (^{16}O or ^{18}O) of μ_4O.

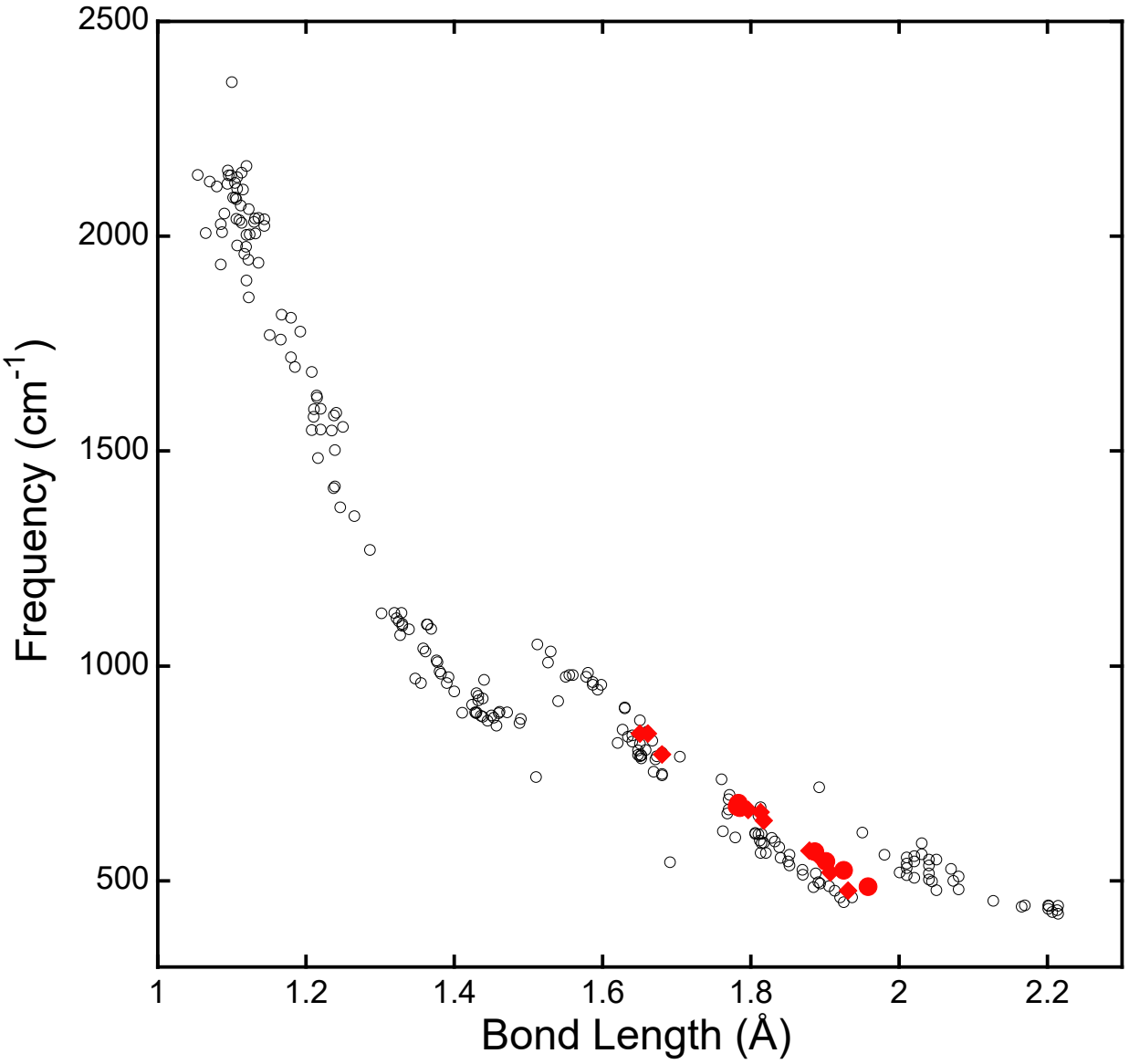

Figure S6. Bond length vs. vibrational frequency plot. All black empty circles are data points reproduced based on a study by Tolman and coworkers [23], the red filled diamonds and circles are experimentally determined and DFT calculated Fe-O/OH stretching frequencies obtained in the current study on the [Fe_4] clusters and a previous study on mononuclear Fe(III) complexes [14], which show a good consistency with all other data.

Reference:

(1) Reed, C. J., and Agapie, T. (2019) A Terminal Fe III –Oxo in a Tetranuclear Cluster: Effects of Distal Metal Centers on Structure and Reactivity. *J. Am. Chem. Soc. 141*, 9479–9484.

(2) Toellner, T. S. (2000) Monochromatization of synchrotron radiation for nuclear resonant scattering experiments. *Hyperfine Interact. 125*, 3–28.

(3) Nakagawa, I., and Shimanouchi, T. (1962) Infrared spectroscopic study on the co-ordination bond-II. *Spectrochim. Acta 18*, 101–113.

(4) Zhao, J. Y., and Sturhahn, W. (2012) High-energy-resolution X-ray monochromator calibration using the detailed-balance principle. *J. Synchrotron Radiat. 19*, 602–608.

(5) Sturhahn, W. (2000) CONUSS and PHOENIX: Evaluation of nuclear resonant scattering data. *Hyperfine Interact. 125*, 149–172.

(6) Frisch, M. J., Trucks, G. W., Schlegel, H. B., Scuseria, G. E., Robb, M. A., Cheeseman, J. R., Scalmani, G., Barone, V., Petersson, G. A., Nakatsuji, H., Li, X., Caricato, M., Marenich, A. V., Bloino, J., Janesko, B. G., Gomperts, R., Mennucci, B., Hratchian, H. P., Ortiz, J. V., Izmaylov, A. F., Sonnenberg, J. L., Williams-Young, D., Ding, F., Lipparini, F., Egidi, F., Goings, J., Peng, B., Petrone, A., Henderson, T., Ranasinghe, D., Zakrzewski, V. G., Gao, J., Rega, N., Zheng, G., Liang, W., Hada, M., Ehara, M., Toyota, K., Fukuda, R., Hasegawa, J., Ishida, M., Nakajima, T., Honda, Y., Kitao, O., Nakai, H., Vreven, T., Throssell, K., Montgomery, J. A., J., Peralta, J. E., Ogliaro, F., Bearpark, M. J., Heyd, J. J., Brothers, E. N., Kudin, K. N., Staroverov, V. N., Keith, T. A., Kobayashi, R., Normand, J., Raghavachari, K., Rendell, A. P., Burant, J. C., Iyengar, S. S., Tomasi, J., Cossi, M., Millam, J. M., Klene, M., Adamo, C., Cammi, R., Ochterski, J. W., Martin, R. L., Morokuma, K., Farkas, O., Foresman, J. B., and Fox, D. J. (2016) Gaussian 16, Revision C.01. Gaussian, Inc., Wallingford CT.

(7) Becke, A. D. (1993) Density-functional thermochemistry. III. The role of exact exchange. *J. Chem. Phys. 98*, 5648.

(8) Lee, C., Yang, W., and Parr, R. G. (1988) Development of the Colle-Salvetti correlation-energy formula into a functional of the electron density. *Phys. Rev. B 37*, 785–789.

(9) Schäfer, A., Horn, H., and Ahlrichs, R. (1992) Fully optimized contracted Gaussian basis sets for atoms Li to Kr. *J. Chem. Phys. 97*, 2571–2577.

(10) Schäfer, A., Huber, C., and Ahlrichs, R. (1994) Fully optimized contracted Gaussian basis sets of triple zeta valence quality for atoms Li to Kr. *J. Chem. Phys. 100*, 5829.

(11) Marenich, A. V., Cramer, C. J., and Truhlar, D. G. (2009) Universal Solvation Model Based on Solute Electron Density and on a Continuum Model of the Solvent Defined by the Bulk Dielectric Constant and Atomic Surface Tensions. *J. Phys. Chem. B 113*, 6378–6396.

(12) Sage, J. T., Paxson, C., Wyllie, G. R. a, Sturhahn, W., Durbin, S. M., Champion, P. M., Alp, E. E., and Scheidt, W. R. (2001) Nuclear resonance vibrational spectroscopy of a protein active-site mimic. *J. Phys. Condens. Matter 13*, 7707–7722.

(13) Chumakov, A. I., Rüffer, R., Leupold, O., and Sergueev, I. (2003) Insight to Dynamics of Molecules with Nuclear Inelastic Scattering. *Struct. Chem. 14*, 109–119.

(14) Weitz, A. C., Hill, E. A., Oswald, V. F., Bominaar, E. L., Borovik, A. S., Hendrich, M. P., and Guo, Y. (2018) Probing Hydrogen Bonding Interactions to Iron-Oxido/Hydroxido Units by 57 Fe Nuclear Resonance Vibrational Spectroscopy. *Angew. Chemie Int. Ed. 57*, 16010–16014.

(15) Gupta, R., and Borovik, A. S. (2003) Monomeric Mn III/II and Fe III/II Complexes with Terminal Hydroxo and Oxo Ligands: Probing Reactivity via O−H Bond Dissociation Energies. *J. Am. Chem. Soc. 125*, 13234–13242.

(16) Parsell, T. H., Yang, M.-Y., and Borovik, A. S. (2009) C−H Bond Cleavage with Reductants: Re-Investigating the Reactivity of Monomeric Mn III/IV −Oxo Complexes and the Role of Oxo Ligand Basicity. *J. Am. Chem. Soc. 131*, 2762–2763.

(17) Parsell, T. H., Behan, R. K., Green, M. T., Hendrich, M. P., and Borovik, A. S. (2006) Preparation and Properties of a Monomeric Mn IV −Oxo Complex. *J. Am. Chem. Soc. 128*, 8728–8729.

(18) Usharani, D., Lacy, D. C., Borovik, A. S., and Shaik, S. (2013) Dichotomous Hydrogen Atom Transfer vs Proton-Coupled Electron Transfer During Activation of X–H Bonds (X = C, N, O) by Nonheme Iron–Oxo Complexes of Variable Basicity. *J. Am. Chem. Soc. 135*, 17090–17104.

(19) Goetz, M. K., and Anderson, J. S. (2019) Experimental Evidence for pKa-Driven Asynchronicity in C–H Activation by a Terminal Co(III)–Oxo Complex. *J. Am. Chem. Soc. 141*, 4051–4062.

(20) Goetz, M. K., and Anderson, J. S. (2020) Correction to "Experimental Evidence for p K a -Driven Asynchronicity in C–H Activation by a Terminal Co(III)–Oxo Complex." *J. Am. Chem. Soc. 142*, 5439–5441.

(21) Goetz, M. K., Hill, E. A., Filatov, A. S., and Anderson, J. S. (2018) Isolation of a Terminal Co(III)-Oxo Complex. *J. Am. Chem. Soc. 140*, 13176–13180.

(22) Dhar, D., and Tolman, W. B. (2015) Hydrogen Atom Abstraction from Hydrocarbons by a Copper(III)-Hydroxide Complex. *J. Am. Chem. Soc. 137*, 1322–1329.

(23) Spaeth, A. D., Gagnon, N. L., Dhar, D., Yee, G. M., and Tolman, W. B. (2017) Determination of the Cu(III)–OH Bond Distance by Resonance Raman Spectroscopy Using a Normalized Version of Badger's Rule. *J. Am. Chem. Soc. 139*, 4477–4485.

(24) Kütt, A., Selberg, S., Kaljurand, I., Tshepelevitsh, S., Heering, A., Darnell, A., Kaupmees, K., Piirsalu, M., and Leito, I. (2018) pKa values in organic chemistry – Making maximum use of the available data. *Tetrahedron Lett. 59*, 3738–3748.